


Tunable spin-wave nonreciprocity in synthetic antiferromagnetic domain walls

Lei Qiu  and Ka Shen*

The Center for Advanced Quantum Studies and Department of Physics, Beijing Normal University, Beijing 100875, China



(Received 20 January 2022; accepted 18 March 2022; published 28 March 2022)

Nonreciprocal propagation of spin waves provides the possibility to design novel functional magnonic devices. In the present paper, based on micromagnetic simulation, we investigate the properties of the spin waves propagating within magnetic domain walls in a synthetic antiferromagnetic bilayer structure and demonstrate a giant frequency nonreciprocity, of which not only the magnitude but also the sign can be efficiently controlled by an external magnetic field. This results from the field-induced modification of the hybridization between the domain-wall spin wave channels from different magnetic layers. The unidirectional excitation of the gigahertz hybridized domain-wall spin waves by a nanostripline antenna is also demonstrated. Our finding suggests the nanoscale antiferromagnetic domain walls should be a promising platform for programmable nonreciprocal spin-wave devices.

DOI: [10.1103/PhysRevB.105.094436](https://doi.org/10.1103/PhysRevB.105.094436)

I. INTRODUCTION

Spin-wave nonreciprocity, usually referred to as the difference in frequency or amplitude between oppositely propagating waves, has recently received intensive study, partially because of its potential applications in spin-wave devices [1–7]. One of the most well-known examples is the unidirectional propagation [1] of the magnetostatic surface spin-wave mode, known as the Damon-Eshbach (DE) mode [8], which is driven by dipolar field.

In the case of a uniform magnetic film, however, the 180° rotation symmetry with respect to the in-plane magnetization guarantees an identical frequency for the DE spin waves with wave vectors of the same magnitude but in opposite directions, although localized separately at the top and bottom surfaces, and thus leads to a reciprocal dispersion relation or the vanishing of frequency nonreciprocity in the entire system. In this sense, it is straightforward to expect the observation of nonreciprocal spin wave dispersion in a magnetic film where this rotation symmetry is broken by a magnetization gradient across the thickness [9] or distinct magnetic anisotropy at the two surfaces [10]. Alternatively, the spin-wave nonreciprocity can also be produced by introducing chiral interactions, e.g., interfacial [11,12] or strain-driven [13,14] Dzyaloshinskii-Moriya interaction (DMI) [15,16], which is responsible for noncollinear spin textures, such as spin spirals and magnetic skyrmions [17–19], and therefore is of particular importance in spintronics [20–23]. Since the DMI-induced frequency difference for the oppositely propagating spin waves depends linearly on the magnitude of their wave vectors [24–27], in practice, the measurements of such a linear dependence via Brillouin light scattering [5,28–31] or spin-wave propagation [6,14,32] are commonly used to evaluate the DMI strength.

Recently, it was shown that such a spin-wave nonreciprocity due to DMI in uniformly magnetized system could be inherited by the confined spin wave propagating modes within the ferromagnetic domain walls [33], i.e., the narrow one-dimensional waveguides between different magnetic domains [34–37]. In the absence of DMI, on the other hand, the domain-wall structure changes from Néel type to Bloch type, where a similar nonreciprocal feature has also been demonstrated [38]. The latter can be understood as the consequence of the dipolar field for the DE-like mode at a single *joint surface* between two ferromagnetic domains. In both cases, the sign of the spin wave nonreciprocity is determined by the chirality of the spin texture and therefore is fixed for an established domain wall, which limits its application in programmable spin-wave devices. To overcome this disadvantage, in the present paper, we propose a scheme to realize highly tunable spin-wave nonreciprocity based on the domain walls in a synthetic antiferromagnetic (SAFM) bilayer system. The key findings are summarized in Fig. 1, where the dispersion relations of the domain-wall spin waves (DWSWs) show a strong dependence on the in-plane magnetic field. The symmetric dispersion in Fig. 1(d) at zero field indicates the vanishing of nonreciprocity, and opposite nonreciprocities are achieved in Figs. 1(c) and 1(e) by reversing the field direction in the simulation.

II. MODEL AND METHOD

To specify our model, we consider a SAFM waveguide consisting of two identical ferromagnetic layers and a spacer of normal metal, where the latter provides an antiferromagnetic exchange coupling between the two ferromagnetic layers through a Ruderman-Kittel-Kasuya-Yosida (RKKY) mechanism [39,40]. For the magnetization dynamics in the gigahertz range, it is proper to use the Hamiltonian

$$H_{\text{tot}} = H_{\text{T}} + H_{\text{B}} + H_{\text{inter}}, \quad (1)$$

*kashen@bnu.edu.cn

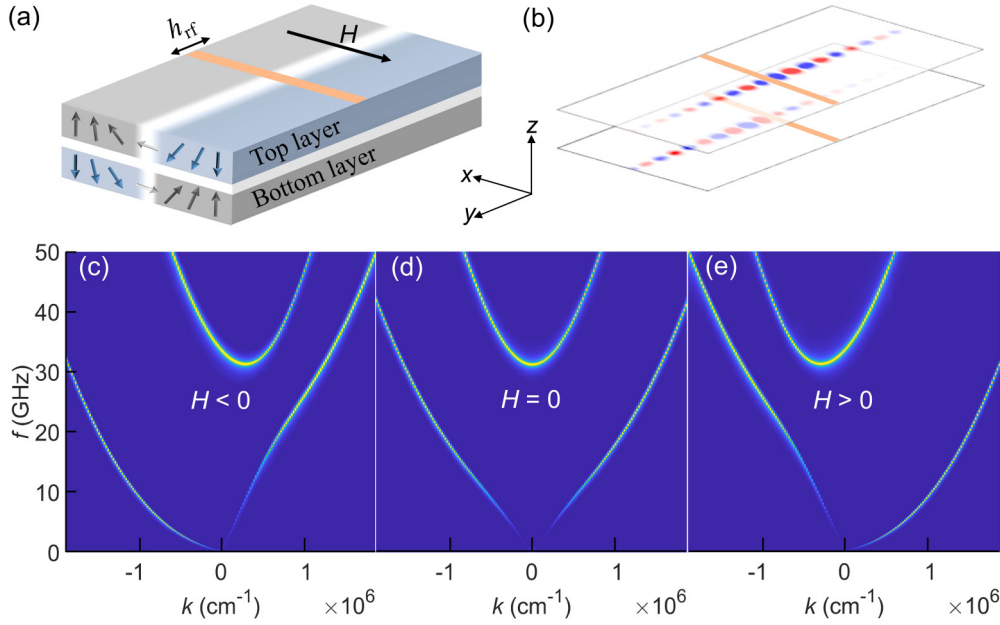


FIG. 1. (a) Schematics of the SAFM domain wall. (b) The DSWs excited by a nanostructure (NSL) antenna lying perpendicular to the domain wall. The dispersion relations of DSWs under an in-plane magnetic field (c) $H < 0$, (d) $H = 0$, and (e) $H > 0$.

where $H_{T(B)}$ and H_{inter} describe the top (bottom) ferromagnetic layer and the RKKY interlayer exchange coupling, respectively.

The Hamiltonian density in the magnetic layer reads

$$\mathcal{H}_\tau = A_{\text{intra}}(\nabla \mathbf{m}_\tau)^2 - K_u(m_\tau^z)^2 - \mu_0 H M_s m_\tau^x + D[m_\tau^z \nabla \cdot \mathbf{m}_\tau - (\mathbf{m}_\tau \cdot \nabla) m_\tau^z], \quad (2)$$

where \mathbf{m}_τ represents the local magnetization orientation with τ being the layer index. The first term of Eq. (2) is the intralayer exchange interaction with the stiffness parameter A_{intra} . The second term with $K_u > 0$ stands for a perpendicular uniaxial magnetic anisotropy and the third term is the Zeeman energy due to the external field applied in x direction. The second line represents the interfacial DMI, with D being the DMI parameter [41]. The areal density of the interlayer exchange coupling due to RKKY mechanism is given by

$$\mathcal{H}_{\text{inter}} = J_{\text{ex}} \mathbf{m}_T \cdot \mathbf{m}_B, \quad (3)$$

where J_{ex} is the interlayer exchange coefficient. In principle, the interfacial DMI and RKKY interaction only exist around the interfaces. In the case the ferromagnetic layers are sufficiently thin, it is safe to apply the approximation to use uniform strengths across the thickness.

The effective field exerting on local magnetization is given by $\mathbf{B}_\tau^{\text{eff}} = -\delta H_{\text{tot}} / (M_s \delta \mathbf{m}_\tau)$, with which the spin-wave dynamics is simulated in MUMAX3 [42] by numerically solving the Landau-Lifshitz-Gilbert equation [43]:

$$\frac{d\mathbf{m}_\tau}{dt} = -\gamma \mathbf{m}_\tau \times \mathbf{B}_\tau^{\text{eff}} + \alpha \mathbf{m}_\tau \times \frac{d\mathbf{m}_\tau}{dt}. \quad (4)$$

Our simulations are performed after discretizing each magnetic layer with $3\text{-}\mu\text{m}$ -long, 256-nm -wide, and 4-nm -thick into $4 \times 2 \times 1 \text{ nm}^3$ unit cells. Periodic boundary condition is applied along the direction of the domain walls. The nanostructure (NSL) antenna at the top of the SAFM structure with

a width of 4 nm is aligned perpendicularly to the domain wall to excite propagating DSWs.

Although our proposal does not rely on the choice of a specific material, the material parameters of a Co/Pt system are adopted according to Refs. [44,45], with the saturation magnetization $M_s = 580 \text{ kA/m}$, the intralayer exchange stiffness $A_{\text{intra}} = 15 \text{ pJ/m}$, the DMI constant $D = 2.5 \text{ mJ/m}^2$, the perpendicular anisotropy parameter $K_u = 0.8 \text{ MJ/m}^3$, and the Gilbert damping coefficient $\alpha = 0.005$, unless otherwise specified. The exchange length with these parameters is estimated to be $l_{\text{ex}} = \sqrt{2A_{\text{intra}} / \mu_0 M_s^2} \simeq 8.4 \text{ nm}$, which is sufficient to ensure the feasibility of our discretization. As the interlayer exchange coefficient J_{ex} depends on the details of the spacer, here we treat it as a free parameter in the range of $0 \sim 2 \text{ mJ/m}^2$. Its positive value is required for establishing the SAFM bilayer, according to Eq. (3).

III. NUMERICAL RESULTS

A. Acoustic and optical DSWs

For a comprehensive understanding of DSWs, we first apply a nonharmonic magnetic field pulse with a sinc-function shape, i.e.,

$$\mathbf{h}(t) = h_0 \text{sinc}(2\pi f_c t) (\hat{y} + \hat{z}), \quad (5)$$

with $\mu_0 h_0 = 1 \text{ mT}$ and $f_c = 200 \text{ GHz}$, to simultaneously excite the spin waves covering a broad frequency band and perform the Fourier transform to the dynamical magnetization. The result in an ideal antiferromagnetic domain wall (without external magnetic field) with interlayer exchange coupling $J_{\text{ex}} = 1 \text{ mJ/m}^2$ is plotted in Fig. 9 in Appendix A, where, in addition to the volume mode, another two modes with distinctive dispersion curves are visible. These modes correspond to the propagating spin waves confined within the SAFM domain wall as shown in Fig. 1(b). While the gapped higher frequency band shows a nice parabolic shape

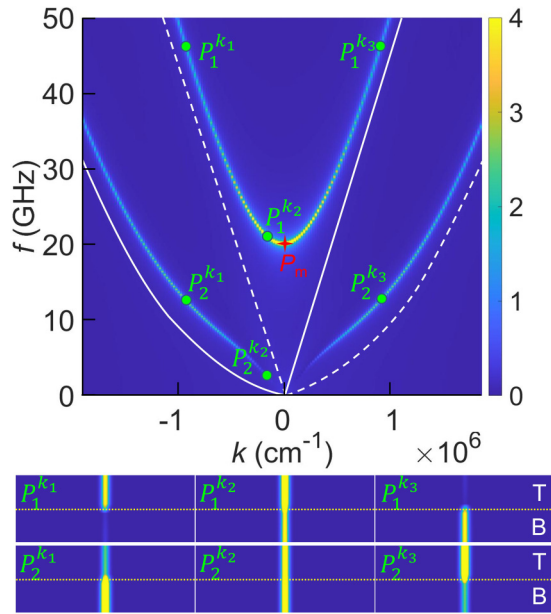


FIG. 2. Upper panel: The spin-wave spectrum of the domain-wall modes with interlayer exchange coupling $J_{\text{ex}} = 0.4 \text{ mJ/m}^2$. The white solid (dashed) curve represents the dispersion curve of the domain-wall mode in an isolated bottom (top) layer, in the absence of interlayer coupling. Lower panel: The amplitude of dynamic magnetization in the cross section of the top (T) and bottom (B) layers in the x - z plane six typical points ($P_i^{k_j}$) in the dispersion curves. P_m stands for the band minimum of the optical branch.

around the band minimum, the gapless band displays a linear dispersion in the long wavelength regime [also see Fig. 1(d)].

The origination of the interesting dispersion features is analyzed in Fig. 2, where the white solid and dashed curves represent the dispersion curves of the DWSW mode in individual bottom and top layers, respectively, in the absence of interlayer coupling [33]. As seen, the inclusion of the interlayer coupling causes a systematic blueshift for large wave vectors, which can be regarded as the consequence of the static exchange field from the antiparallel aligning local magnetization in the other layer. The figures in the lower panel of Fig. 2 plot the cross-section profile of the amplitude of dynamic magnetization. For those at the large wave-vector states $P_{1(2)}^{k_1}$ and $P_{2(1)}^{k_3}$, the magnetization dynamics indeed mainly occurs at the top (bottom) layer. The situation for the long wavelength states $P_{1(2)}^{k_2}$ are, however, quite different. Both layers almost equally contribute to the propagating modes, indicating the hybridization of the two DWSW channels in the top and bottom magnetic layers. This also explains the strong modification of dispersion curves in this region compared to the uncoupled DWSW modes.

To clarify the dynamics of these two modes, we replace the sinc-function pulse by a continuously sinusoidal function with selected frequency to excite the two hybridized domain-wall modes. In practice, we take 1 GHz for the excitation of the low-frequency band in the linear dispersion region. For the excitation of the long wavelength state of the higher frequency mode, the frequency was chosen to be the one at its band minimum, i.e., 20.2 GHz. A wide antenna of 600 nm is used to

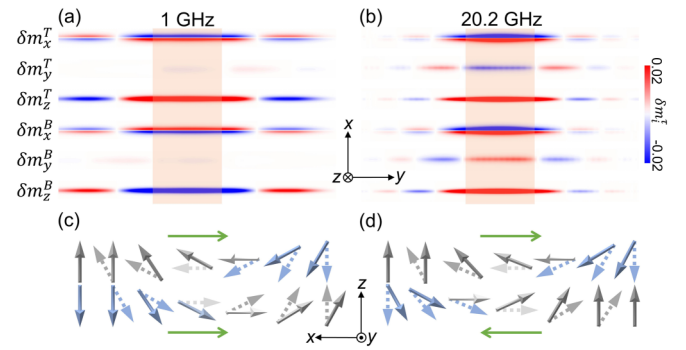


FIG. 3. (a), (b) Spatial profile of the long wavelength DWSWs excited by a 600-nm-wide antenna (represented by the orange area) at the frequencies of 1 and 20.2 GHz, respectively. Instantaneous spin configurations beneath the antenna for (c) acoustic and (d) optical DWSW modes (solid arrows) and those at the equilibrium state (dashed arrows). The olive arrows show the direction of the local domain-wall motion in each layer.

suppress the influence from the short-wavelength spin waves from the lower band with the same frequency. The spatial profiles of an instantaneous magnetization are plotted in Fig. 3. The low frequency dynamics in Fig. 3(a) reveals the synchronized motion of the domain walls in the top and bottom layers, as shown in Fig. 3(c), which approximately maintains the local antiferromagnetic configuration. The in-plane translation symmetry with respect to a transverse displacement of the domain wall leads to a vanishing frequency at $k = 0$ and the linear dispersion around as a Goldstone mode or acoustic DWSW, and the negligible dynamical magnetization of this Goldstone mode also explains the inefficiency of the excitation at very low frequency regime in the vicinity of $k = 0$ in Fig. 2. As illustrated in Fig. 3(d), the higher frequency mode shown in Fig. 3(b), on the other hand, contains a relative movement between the top and bottom domain walls, corresponding to an optical DWSW mode, with an oscillating local magnetization allowing high efficient excitation.

B. Field-induced nonreciprocity of the acoustic mode

According to Ref. [33], the DMI can lead to nonreciprocal spin-wave propagation in the domain wall of single magnetic layer, which can also be seen from the solid or dashed curves in Fig. 2. Due to the opposite chirality of the top layer with respect to the bottom one, its nonreciprocity is inverted [33]. As a result, in the ideal bilayer SAFM, the combination of the two sets of dispersion makes a symmetric spectrum and hence the vanishing of nonreciprocity, which is valid also in the presence of the interlayer coupling. Following this discussion, one may expect to reproduce the nonreciprocity by, for example, introducing a difference between the material parameters in the two layers to break the ideal symmetry of SAFM. Alternatively, in this paper, we consider an easier and more applicable way by modifying the equilibrium spin configurations in the two layers via an external magnetic field.

As illustrated in Figs. 4(a) and 4(b), the antiferromagnetic nature is broken by an in-plane magnetic field in the x direction, i.e., perpendicular to the domain wall, which shrinks or broadens the domain walls in the top and bottom layers,

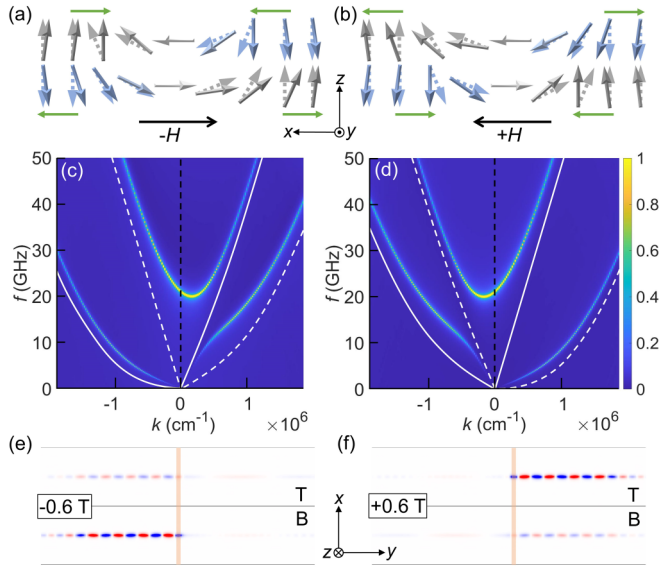


FIG. 4. The static spin configurations (solid arrows) under (a) positive and (b) negative magnetic field along x direction and (c), (d) the resulting spin wave spectra with $J_{\text{ex}} = 0.4 \text{ mJ/m}^2$. The olive arrows indicate the displacement of domain wall boundary with respect to the zero-field spin configurations (dashed arrows). The white solid and dashed curves in (c), (d) stand for the domain-wall modes in the bottom and top layers separately at vanishing interlayer coupling. (e), (f) Snapshots of dynamic magnetization excited at the frequency of 2 GHz at $\mu_0 H = \pm 0.6 \text{ T}$.

respectively. The difference between the effective widths of the domain walls in the two magnetic layers linearly depends on the magnetic field, see Fig. 10 in Appendix B. As a consequence, the spin-wave dispersion relations in Figs. 4(c) and 4(d) become asymmetric with respect to $k = 0$, reflecting the existence of frequency nonreciprocity. The field-induced spectrum distortion can be well understood by the white curves, which, similar to those in Fig. 2, represent the dispersion relations of the DWSW modes in uncoupled two layers. Specifically, for $H_x < 0$, the frequency of the DWSW in the isolated bottom layer (represented by solid curves) is depressed while that in the top layer (represented by dashed curves) is lifted up, resulting from the different changes of effective widths of domain walls in the two layers because, according to Ref. [33], the frequency of the DWSW increases (decreases) with the decrease (increase) of the domain wall width. As a result, in the positive wave-vector regime, the modification due to the interlayer coupling is enhanced thanks to the reduction of the frequency difference between the top and bottom DWSW modes. In contrast, the interlayer coupling shows a weaker effect in the negative wave vector regime. Things are reversed for $H_x > 0$.

Moreover, in the presence of the external magnetic field, the spin-wave spectra shown in Figs. 4(c) and 4(d) also show a clear nonreciprocity between the amplitudes of the excited spin waves with opposite wave vectors, especially in the low-frequency part. This reflects the different magnitudes of oscillating magnetization in the DWSWs propagating in opposite directions. This feature is also seen from the simulation with a continuous excitation at 2 GHz, as plotted in

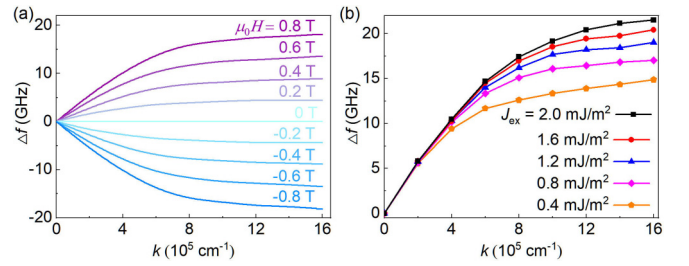


FIG. 5. Frequency nonreciprocity as function of wave vector (a) under different values of external magnetic field at $J_{\text{ex}} = 1 \text{ mJ/m}^2$ and (b) with different interlayer coupling under the magnetic field at $\mu_0 H = 0.8 \text{ T}$.

Figs. 4(e) and 4(f), where the excited spin waves show nearly a unidirectional propagation.

Focusing on the acoustic DWSW mode, the frequency nonreciprocity, i.e., the frequency difference of channeled spin waves with opposite wave vectors

$$\Delta f = f(+k) - f(-k), \quad (6)$$

is plotted in Fig. 5(a) as function of the magnitude of wave vectors at different values of magnetic field. For a given magnetic field, the magnitude of the frequency nonreciprocity first increases linearly with the increase of the wave vector in the strong coupling, and the slope gradually becomes gentler in the large wave-vector regime, where the intermode coupling is relatively weak, and the sign of the frequency nonreciprocity is determined by the direction of the external magnetic field. Figure 5(b) shows the dependence of frequency nonreciprocity on the strength of the interlayer antiferromagnetic coupling, which mainly affects the large wave-vector states in the weak coupling regime. This can also be seen from Fig. 4(c), in which the acoustic mode shifts upward from the uncoupled dispersion (white curves) with a larger magnitude for $k > 0$. Notice also that the optical mode behaves in the opposite way. However, if we reconsider this frequency shift with respect to the spatial distribution of the oscillating magnetic moments, it turns out that the top-layer-dominating spin wave gains a larger frequency shift from the interlayer coupling than the bottom-layer-dominating one. This can be attributed to the change in the domain-wall widths of the two layers since the domain wall in the top layer is narrower than that in the bottom layer. The rotating magnetic moments for the DWSW in the top-layer domain wall all feel a background exchange field from the domain wall in the bottom layer. In contrast, only part of the dynamic magnetic moments can feel the exchange field from the top-layer domain wall, reducing the average value of the static exchange field.

Figure 6 summarizes the group velocities for the left- ($-k$) and right-moving ($+k$) DWSWs at zero magnetic field and 0.4 T. At zero field, their magnitudes are always equal, because of the symmetric spin-wave spectrum. As the frequency increases, the group velocity first gradually decreases and then increases, displaying a nonmonotonic behavior. The minimum reflects the crossover between the strong coupled regime with linear dispersion and the weak coupling regime at higher frequencies, see Figs. 1(d) and 2. With an applied magnetic field, the minimal group velocities for the left- and right-moving

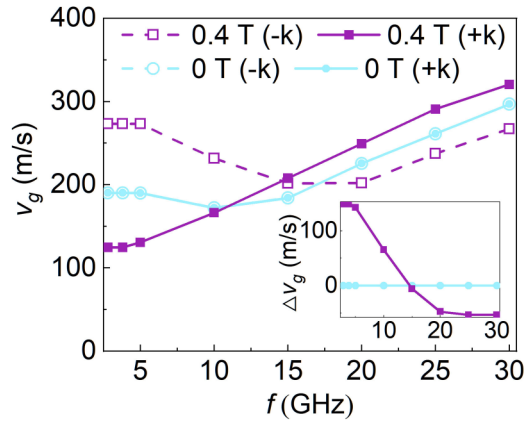


FIG. 6. Group velocities of the left- and right-moving ($-k$ and $+k$) waves as function of frequency with zero (light blue symbols) and 0.4 T (purple symbols) magnetic field. In this calculation, we take $J_{\text{ex}} = 1 \text{ mJ/m}^2$.

waves shift to higher and lower frequencies, respectively. At 0.4 T, shown by the purple symbols in Fig. 6, the velocity of the right-moving wave becomes almost monotonic, and its value is smaller (larger) than the left-moving wave in the low (high) frequency regime. Their difference plotted as the inset therefore shows a sign change.

C. Influence on the optical mode

From the spin wave spectra in Figs. 4(c) and 4(d), we also observe a distortion in the optical DWSW mode with a higher frequency compared to its zero-field spectrum in Fig. 2. Its band minimum P_m shifts to a finite wave vector k_m . In Fig. 7, the wave vector k_m and the corresponding spin wave gap f_m , i.e., the frequency of the band minimum, are plotted as a function of the magnetic field, the interlayer exchange coupling, and the DMI strength. In Fig. 7(a) with fixed exchange and DMI strength, k_m shows a linear dependence on the magnetic field in the range from -0.8 T to $+0.8 \text{ T}$, while f_m is found to be insensitive to the magnetic field. Qualitatively, the latter might be caused by the competition between two effects. On one hand, f_m tends to increase when the optical band minimum is shifted to a finite wave vector by the magnetic field. On the other hand, the different modifications of the domain walls in the two layers will suppress the overlap between the DWSW modes therein, which results in a decrease in the coupling between the DWSW modes and hence a smaller anticrossing gap between the hybridized acoustic and optical modes, preventing the increase of f_m , and, in Fig. 7(b) with fixed DMI strength and a constant magnetic field $\mu_0 H = \pm 0.8 \text{ T}$, the frequency of P_m increases with increasing J_{ex} , which can be understood easily from the fact that the spin wave gap is directly opened by the interlayer coupling. The size of the gap is more sensitive to the exchange strength in the weak coupling regime, where the shift of band minimum k_m also shows a stronger dependence on the interlayer coupling. According to Fig. 7(c), the influence of DMI strength on the spin-wave gap looks very similar to that of the interlayer coupling. The gap tends to vanish in the weak DMI limit $D \simeq 0$. This means that the size of the gap is actually determined

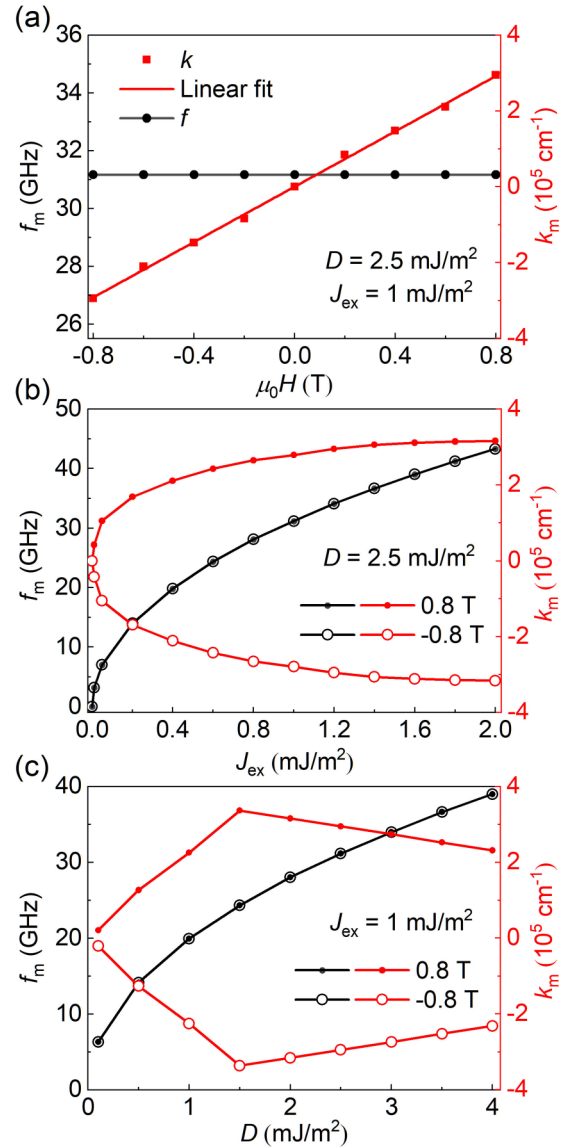


FIG. 7. Spin-wave gap and the shift of band minimum of the optical DWSW as function of (a) the external magnetic field, (b) the interlayer exchange coupling, and (c) the DMI strength.

by the combination of the interlayer coupling and the DMI. Note that the Néel-type domain wall becomes unstable at very weak DMI, which prohibits the simulation around the zero DMI limit. The wave vector k_m , on the other hand, shows a nonmonotonic behavior. It increases from zero and then decreases as the DMI strength increases.

To explain the nonmonotonic dependence of k_m on DMI strength, as shown in Fig. 8, we plot the spin-wave spectra with three typical DMI strengths. With an intermediate DMI strength around the crossover regime $D = 2 \text{ mJ/m}^2$, close to the value used in other calculations, a significant asymmetry with a large k_m is visible in the spectrum. With a stronger DMI $D = 4 \text{ mJ/m}^2$, the enhancement of the nonreciprocity in two isolated layers makes the solid and dashed curves with roughly linear dispersion relations closer with each other, which pushes k_m to a smaller value. In the opposite limit, with a weak DMI $D = 0.5 \text{ mJ/m}^2$, the spin-wave spectrum reduces

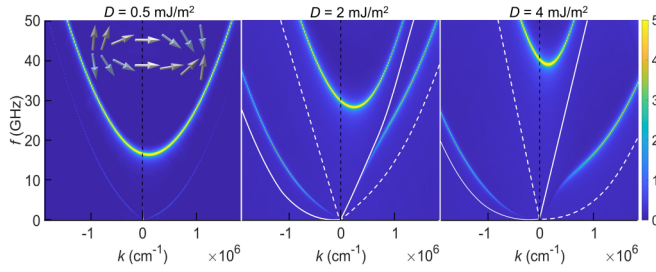


FIG. 8. DWSW spectra with different DMI strengths. In the calculation, the interlayer exchange parameter and the magnetic field are taken to be $J_{\text{ex}} = 1 \text{ mJ/m}^2$ and $\mu_0 H = -0.8 \text{ T}$.

to be almost symmetric, as the nonreciprocity originates from the DMI. It is noteworthy that the chirality of the top domain wall as shown in the inset, compared to the spin texture in Fig. 4(a), is switched by the external field, which is sufficiently strong to overcome the potential barrier of the chiral domain wall due to DMI.

It is worth pointing out that in the case of a Bloch-type antiferromagnetic domain wall, an applied magnetic field along the domain wall modifies the domain-wall profile in a very similar way and therefore the mechanism proposed here also works as confirmed by our numerical calculation. Such a dipolar-field-associated nonreciprocity is however rather weak.

IV. SUMMARY

In summary, we performed micromagnetic simulation to investigate the channeled spin-wave modes propagating within the domain walls in an antiferromagnetic coupled magnetic bilayer. Thanks to the interlayer coupling, the DWSW modes in different magnetic layers become hybridized and result in one gapless acoustic mode with linear dispersion and the other gapped optical one. Although the spin-wave spectrum is symmetric at zero field, the presence of an in-plane

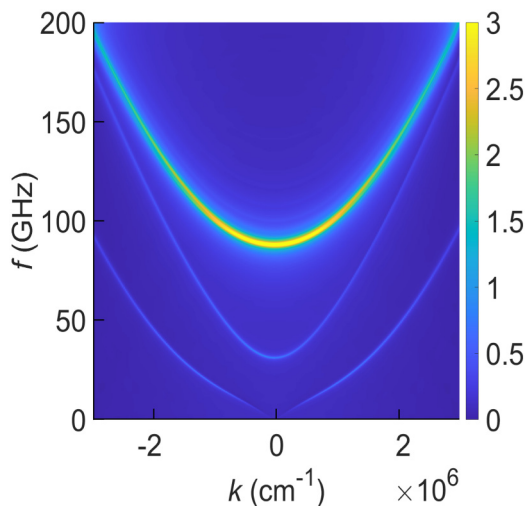


FIG. 9. Zero-field spin wave spectrum with the interlayer exchange parameter $J_{\text{ex}} = 1 \text{ mJ/m}^2$ and the DMI strength $D = 2.5 \text{ mJ/m}^2$.

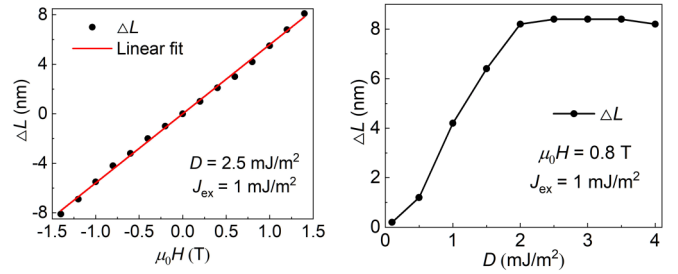


FIG. 10. Difference between the effective widths of the top and bottom domain walls as function of (left panel) the external magnetic field and (right panel) the DMI strength.

magnetic field causes a large distortion to the spin-wave spectrum and introduces not only a giant frequency nonreciprocity but also unidirectional excitation by NSL antenna, originating from the modification of the spin texture by the magnetic field. The field-controllable nonreciprocity of the gapped optical mode was also analyzed.

Finally, we should point out that, although we only presented the results in an ideal SAFM bilayer structure with two identical magnetic layers, our key finding of field-tunable spin-wave nonreciprocity was also verified in other general cases, for example, with different DMI strengths 2 mJ/m^2 and 3 mJ/m^2 in the top and bottom layers. As an extension to field-free devices, one could introduce an in-plane magnetized layer coupled to one of the magnetic layers in the SAFM bilayer, so the nonreciprocity can be controlled by electrically switching the magnetization direction in this third layer.

ACKNOWLEDGMENTS

This work is supported by the National Natural Science Foundation of China (Grant No.11974047) and the Fundamental Research Funds for the Central Universities.

APPENDIX A: SPIN WAVE SPECTRUM WITH BOTH VOLUME AND DOMAIN WALL MODES

For the calculation of the zero-field spin wave spectrum in Fig. 9, we use interlayer exchange coupling $J_{\text{ex}} = 1 \text{ mJ/m}^2$ and DMI strength $D = 2.5 \text{ mJ/m}^2$. The local excitation with sinc-function pulse is applied to excite the SAFM including a domain wall, as explained in the main text. While the spin-wave spectra in the main text are obtained from the Fourier transform of the out-of-plane component of the dynamical magnetization m_z , here, to show the volume mode, we use the in-plane component m_y instead. The brightest branch corresponds to the volume mode and the other two darker branches with lower frequencies are spin waves propagating within the domain walls.

APPENDIX B: DIFFERENCE BETWEEN THE DOMAIN-WALL WIDTHS IN THE TOP AND BOTTOM LAYERS

In the presence of the in-plane magnetic field, the magnetization profile deviates from the Walker solution [46],

therefore, we define an effective domain-wall width as the distance between the positions of the magnetic moments with 45° and 135° angles with respect to the out-of-plane direction. With L_T and L_B separately representing the domain-wall widths in the top and bottom layers, the difference between them $\Delta L = L_T - L_B$ is plotted in Fig. 10 as a function of the magnetic field and the DMI strength. With a fixed DMI strength and a constant interlayer exchange interlayer coupling, ΔL varies linearly with the external magnetic field. For a fixed external field and a constant interlayer exchange

coupling, ΔL first increases with DMI strength and gets saturated. The saturation at the larger DMI regime can be understood from the fact that once the antiferromagnetic domain wall is established with a sufficiently strong DMI, ΔL is mainly determined by the competition between the interlayer exchange coupling and the Zeeman term, which prefer the antiparallel and parallel alignments of spins in the two layers, respectively. If the DMI is too weaker, the antiferromagnetic domain wall will be destroyed by the external field, as shown by the inset of Fig. 8(a).

- [1] T. An, V. I. Vasyuchka, K. Uchida, A. V. Chumak, K. Yamaguchi, K. Harii, M. B. Ohe, J. Jungfleisch, Y. Kajiwara, H. Adachi, B. Hillebrands, S. Maekawa, and E. Saitoh, *Nat. Mater.* **12**, 549 (2013).
- [2] M. Jamali, J. H. Kwon, S.-M. Seo, K.-J. Lee, and H. Yang, *Sci. Rep.* **3**, 3160 (2013).
- [3] J. Chen, T. Yu, C. Liu, T. Liu, M. Madami, K. Shen, J. Zhang, S. Tu, M. S. Alam, K. Xia, M. Wu, G. Gubbiotti, Y. M. Blanter, G. E. W. Bauer, and H. Yu, *Phys. Rev. B* **100**, 104427 (2019).
- [4] K. Zakeri, Y. Zhang, J. Prokop, T.-H. Chuang, N. Sakr, W. X. Tang, and J. Kirschner, *Phys. Rev. Lett.* **104**, 137203 (2010).
- [5] K. Di, V. L. Zhang, H. S. Lim, S. C. Ng, M. H. Kuok, J. Yu, J. Yoon, X. Qiu, and H. Yang, *Phys. Rev. Lett.* **114**, 047201 (2015).
- [6] H. Wang, J. Chen, T. Liu, J. Zhang, K. Baumgaertl, C. Guo, Y. Li, C. Liu, P. Che, S. Tu, S. Liu, P. Gao, X. Han, D. Yu, M. Wu, D. Grundler, and H. Yu, *Phys. Rev. Lett.* **124**, 027203 (2020).
- [7] J. Han, Y. Fan, B. C. McGoldrick, J. Finley, J. T. Hou, P. Zhang, and L. Liu, *Nano Lett.* **21**, 7037 (2021).
- [8] R. Damon and J. Eshbach, *J. Phys. Chem. Solids* **19**, 308 (1961).
- [9] R. A. Gallardo, P. Alvarado-Seguel, T. Schneider, C. Gonzalez-Fuentes, A. Roldán-Molina, K. Lenz, J. Lindner, and P. Landeros, *New J. Phys.* **21**, 033026 (2019).
- [10] O. Gladii, M. Haidar, Y. Henry, M. Kostylev, and M. Bailleul, *Phys. Rev. B* **93**, 054430 (2016).
- [11] A. R. Fert, *Mater. Sci. Forum* **59-60**, 439 (1990).
- [12] M. Bode, M. Heide, K. von Bergmann, P. Ferriani, S. Heinze, G. Bihlmayer, A. Kubetzka, O. Pietzsch, S. Blügel, and R. Wiesendanger, *Nature (London)* **447**, 190 (2007).
- [13] D. A. Kitchaev, I. J. Beyerlein, and A. Van der Ven, *Phys. Rev. B* **98**, 214414 (2018).
- [14] Y. Zhang, J. Liu, Y. Dong, S. Wu, J. Zhang, J. Wang, J. Lu, A. Rückriegel, H. Wang, R. Duine, H. Yu, Z. Luo, K. Shen, and J. Zhang, *Phys. Rev. Lett.* **127**, 117204 (2021).
- [15] T. Moriya, *Phys. Rev.* **120**, 91 (1960).
- [16] I. Dzyaloshinsky, *J. Phys. Chem. Solids* **4**, 241 (1958).
- [17] A. Fert, N. Reyren, and V. Cros, *Nat. Rev. Mater.* **2**, 17031 (2017).
- [18] N. Nagaosa and Y. Tokura, *Nat. Nanotechnol.* **8**, 899 (2013).
- [19] K. Everschor-Sitte, J. Masell, R. M. Reeve, and M. Kläui, *J. Appl. Phys.* **124**, 240901 (2018).
- [20] W. Wang, M. Albert, M. Beg, M.-A. Bisotti, D. Chernyshenko, D. Cortés-Ortuño, I. Hawke, and H. Fangohr, *Phys. Rev. Lett.* **114**, 087203 (2015).
- [21] K.-W. Kim, S.-W. Lee, J.-H. Moon, G. Go, A. Manchon, H.-W. Lee, K. Everschor-Sitte, and K.-J. Lee, *Phys. Rev. Lett.* **122**, 147202 (2019).
- [22] H. Yu, J. Xiao, and H. Schultheiss, *Phys. Rep.* **905**, 1 (2021).
- [23] A. Qaiumzadeh, L. A. Kristiansen, and A. Brataas, *Phys. Rev. B* **97**, 020402(R) (2018).
- [24] J.-H. Moon, S.-M. Seo, K.-J. Lee, K.-W. Kim, J. Ryu, H.-W. Lee, R. D. McMichael, and M. D. Stiles, *Phys. Rev. B* **88**, 184404 (2013).
- [25] F. J. dos Santos, M. dos Santos Dias, and S. Lounis, *Phys. Rev. B* **102**, 104401 (2020).
- [26] G. Gitgeatpong, Y. Zhao, P. Piyawongwatthana, Y. Qiu, L. W. Harriger, N. P. Butch, T. J. Sato, and K. Matan, *Phys. Rev. Lett.* **119**, 047201 (2017).
- [27] L. Udvardi and L. Szunyogh, *Phys. Rev. Lett.* **102**, 207204 (2009).
- [28] J. Cho, N.-H. Kim, S. Lee, J.-S. Kim, R. Lavrijsen, A. Solignac, Y. Yin, D.-S. Han, N. J. J. van Hoof, H. J. M. Swagten, B. Koopmans, and C.-Y. You, *Nat. Commun.* **6**, 7635 (2015).
- [29] H. T. Nembach, J. M. Shaw, M. Weiler, E. Jué, and T. J. Silva, *Nat. Phys.* **11**, 825 (2015).
- [30] M. Belmuguenai, J.-P. Adam, Y. Roussigné, S. Eimer, T. Devolder, J.-V. Kim, S. M. Cherif, A. Stashkevich, and A. Thiaville, *Phys. Rev. B* **91**, 180405(R) (2015).
- [31] S. Tacchi, R. E. Troncoso, M. Ahlberg, G. Gubbiotti, M. Madami, J. Åkerman, and P. Landeros, *Phys. Rev. Lett.* **118**, 147201 (2017).
- [32] J. M. Lee, C. Jang, B.-C. Min, S.-W. Lee, K.-J. Lee, and J. Chang, *Nano Lett.* **16**, 62 (2016).
- [33] F. Garcia-Sanchez, P. Borys, R. Soucaille, J.-P. Adam, R. L. Stamps, and J.-V. Kim, *Phys. Rev. Lett.* **114**, 247206 (2015).
- [34] K. Wagner, A. Kákay, K. Schultheiss, A. Henschke, T. Sebastian, and H. Schultheiss, *Nat. Nanotechnol.* **11**, 432 (2016).
- [35] E. Albisetti, D. Petti, G. Sala, R. Silvani, S. Tacchi, S. Finizio, S. Wintz, A. Calò, X. Zheng, J. Raabe, E. Riedo, and R. Bertacco, *Commun. Phys.* **1**, 56 (2018).
- [36] X. Xing and Y. Zhou, *NPG Asia Mater* **8**, e246 (2016).
- [37] Q. Wang, B. Heinz, R. Verba, M. Kewenig, P. Pirro, M. Schneider, T. Meyer, B. Lägél, C. Dubs, T. Brächer, and A. V. Chumak, *Phys. Rev. Lett.* **122**, 247202 (2019).
- [38] Y. Henry, D. Stoeffler, J.-V. Kim, and M. Bailleul, *Phys. Rev. B* **100**, 024416 (2019).

- [39] S. S. P. Parkin, R. Bhadra, and K. P. Roche, *Phys. Rev. Lett.* **66**, 2152 (1991).
- [40] W. Legrand, D. Maccariello, F. Ajejas, S. Collin, A. Vecchiola, K. Bouzehouane, N. Reyren, V. Cros, and A. Fert, *Nat. Mater.* **19**, 34 (2020).
- [41] R. Tomasello, E. Martinez, R. Zivieri, L. Torres, M. Carpentieri, and G. Finocchio, *Sci. Rep.* **4**, 6784 (2015).
- [42] A. Vansteenkiste, J. Leliaert, M. Dvornik, M. Helsen, F. Garcia-Sanchez, and B. Van Waeyenberge, *AIP Adv.* **4**, 107133 (2014).
- [43] T. Gilbert, *Phys. Rev.* **100**, 1243 (1955).
- [44] J. Sampaio, V. Cros, S. Rohart, A. Thiaville, and A. Fert, *Nat. Nanotechnol.* **8**, 839 (2013).
- [45] A. Fert, V. Cros, and J. Sampaio, *Nat. Nanotechnol.* **8**, 152 (2013).
- [46] N. L. Schryer and L. R. Walker, *J. Appl. Phys.* **45**, 5406 (1974).